INTERNATIONAL JOURNAL OF REMOTE SENSING, 2018
VOL. 39, NO. 8, 2399–2420
https://doi.org/10.1080/01431161.2017.1420935

Taylor & Francis
Taylor & Francis Group

The potential use of geostationary MTG/FCI to retrieve chlorophyll-*a* concentration at high temporal resolution for the open oceans

Héloïse Lavigne[a] and Kevin Ruddick[a]

[a]Royal Belgian Institute of Natural Sciences, Operational Directorate Natural Environment, Brussels, Belgium

ABSTRACT

In a few years, the Flexible Combined Imager (FCI) on-board Meteosat Third Generation will provide images of European Seas, the Atlantic Ocean, and the Mediterranean Sea every 2.5 min (regions above 30° N) or 10 min (full disk). Although dedicated to meteorological applications, this sensor has blue, green, and red spectral bands allowing to consider the adaptation of a band-ratio algorithm to retrieve chlorophyll-*a* concentration (chl-*a*). However, the radiometric specification of the FCI sensor is far from the minimum requirement recommended for ocean colour sensors and the validity of FCI data for oceanic applications is not clear. This present article aims to determine if, and under which conditions, chl-*a* could be estimated from FCI data. From the National Aeronautics and Space Administration bio-Optical Marine Algorithm data set *in situ* data set, a blue green band-ratio algorithm adapted to FCI spectral characteristics is proposed. Then, the impact of FCI radiometric noise on chl-*a* estimations is investigated in detail. Results show that noise-induced chl-*a* error increases with chl-*a* and solar zenith angle. For a chl-*a* estimation based on a unique pixel, this error ranges between 20% and 100% which prevents any direct utilisation and suggests that it is necessary to degrade the spatio-temporal resolution to obtain an acceptable noise-related uncertainty on chl-*a*. With a spatial (9 pixels) and temporal (1 h) averaging process, chl-*a* can be estimated with a noise-induced error less than 10% for chl-*a* up to 5 mg m^{-3} and solar zenith angle lower than 60°. Our analysis also showed that the noise-related error associated to the atmospheric correction process can be neglected compared to the radiometric noise of the visible bands themselves if it is assumed that aerosol type is uniform over large areas (9 km × 9 km boxes).

ARTICLE HISTORY
Received 26 June 2017
Accepted 7 December 2017

1. Introduction

Satellite sensors dedicated to ocean colour, as for example the Moderate Resolution Imaging Spectroradiometer (MODIS) or the Medium Resolution Imaging Spectrometer, have made important contributions to our understanding of oceanic ecosystems and biogeochemical carbon cycles (IOCCG 2008). Most of these sensors are installed on Sun

CONTACT Héloïse Lavigne hlavigne@naturalsciences.be

synchronous polar orbiting platforms which provide a global coverage of the planet within 2 days. Hence, the revisit-period varies from 1 to 2 days depending on the latitude and swath. However, the cloud coverage can significantly increase the time gap between two consecutive observations preventing adequate monitoring of surface bio-optical properties and ecosystem dynamics. For instance, phytoplankton blooms, commonly monitored from space via surface chlorophyll-*a* concentration (chl-*a* hereafter), are highly dynamic and are sometime characterised by very short-term events (Smayda 1998). The lack of data in satellite based chl-*a* time-series can then lead to a misunderstanding of the phytoplankton phenology (Cole et al., 2012) or even fully mask the seasonal bloom (Taylor et al. 2006). In addition, only one observation per day does not allow resolving diurnal variability of bio-optical and biogeochemical properties which are driven by the diel cycle of solar irradiance (Loisel et al. 2011; Gernez, Antoine, and Huot 2011; IOCCG 2012a) and, in coastal regions, by tides (Neukermans, Ruddick, and Greenwood 2012). Yet, a good understanding of diurnal variability of these variables is necessary to better assess marine environments. In particular, it was shown that knowing the variations of phytoplankton biomass during the day is necessary for an improved estimation of daily primary production (Lee et al. 2012).

One way to remove this limitation for low and middle latitudes is to use a sensor on a platform in geostationary orbit (Geo; Ruddick et al. 2014; IOCCG 2012a). Although Geo sensors only cover a part of the Earth, they can provide images with high temporal frequency, typically one image per hour. Currently, the only Geo sensor dedicated to ocean colour application is the Geostationary Ocean Colour Imager (Ryu et al. 2012). It provides images every hour with a spatial resolution of 500 m for eight spectral bands in the visible range but its field of view is restricted to the Korean Peninsula and surrounding seas (Yellow Sea, Sea of Japan, East China Sea). In the other regions, only Geo sensors dedicated to meteorological applications are available. Over European seas, Neukermans et al. (2009, 2012) demonstrated that the Spinning Enhanced Visible and Infra-red Imager (SEVIRI) on-board Meteosat Second Generation (MSG) can be used for marine applications. Indeed, those studies showed that in turbid waters, the water leaving signal is high enough for retrieval of tidal variations of suspended particulate matter (SPM) and turbidity even with a sensor with a low signal-to-noise ratio (SNR). Recently, Murakami (2016) demonstrated that, the blue, green, and red spectral bands of the Advance Himawari Imager (AHI) sensor on-board the Meteorological Satellite Himawari-8 allow to retrieve chl-*a* in open waters from band-ratio algorithms. However, the associated error that depends on solar and sensor geometry and on water properties is rather high.

The next generation of European meteorological satellites (Meteosat Third Generation, MTG) should operate between 2019 and 2039 and will be equipped with the Flexible Combined Imager (FCI). This sensor presents some similarities with AHI and is an improvement of SEVIRI regarding spatio-temporal resolution as well as spectral and radiometric characteristics (Table 1, EURD, 2010). All FCI visible bands will have a spatial resolution of 1 km at nadir and temporal resolution will depend on the scanning mode: Full Disc Scanning Service (FDSS) or Rapid Scan Service (RSS). In the FDSS mode, the whole disk is scanned whereas if the RSS mode is chosen only a subset of the full disk called local area coverage (northern part of the disk, see yellow area on Figure 1) is scanned. If the RSS and FDSS mode are conducted in parallel with two satellites, the

Table 1. Spectral and radiometric characteristics of the FCI and SEVIRI channels in vis, NIR, and SWIR (information reported from the EURD document 2010, and from EUM/MSG/ICD/105 2013).

Sensor	Channel	λ_0 (μm)	$\Delta\lambda_0$ (μm)	α_{ref}	α_{min}	α_{max}	SNR_{ref}
FCI	Vis0.4	0.444	0.060	0.01	0.01	1.20	>25
FCI	Vis0.5	0.510	0.040	0.01	0.01	1.20	>25
FCI	Vis0.6	0.640	0.050	0.01	0.01	1.20	>30
FCI	NIR0.8	0.865	0.040	0.01	0.01	1.20	>21
FCI	NIR0.9	0.914	0.020	0.01	0.01	0.80	>12
FCI	SWIR1.3	1.380	0.030	0.01	0.01	0.80	>40
FCI	SWIR1.6	1.610	0.050	0.01	0.01	1.00	>30
FCI	SWIR2.2	2.250	0.050	0.01	0.01	1.00	>25
SEVIRI	Vis0.6	0.635	0.150	0.01	0	1.00	>10.1
SEVIRI	Vis0.8	0.810	0.140	0.01	0	1.00	>7.8
SEVIRI	SWIR1.6	1.640	0.280	0.01	0	1.00	>3

λ_0 is for the central wavelength and $\Delta\lambda_0$ (full width half max) the spectral width. α_{ref}, α_{min}, and α_{max} refers to the reference, minimum, and maximum signal, respectively. α represents the TOA reflectance multiplied by the cosine of the solar zenith angle (see text for details).

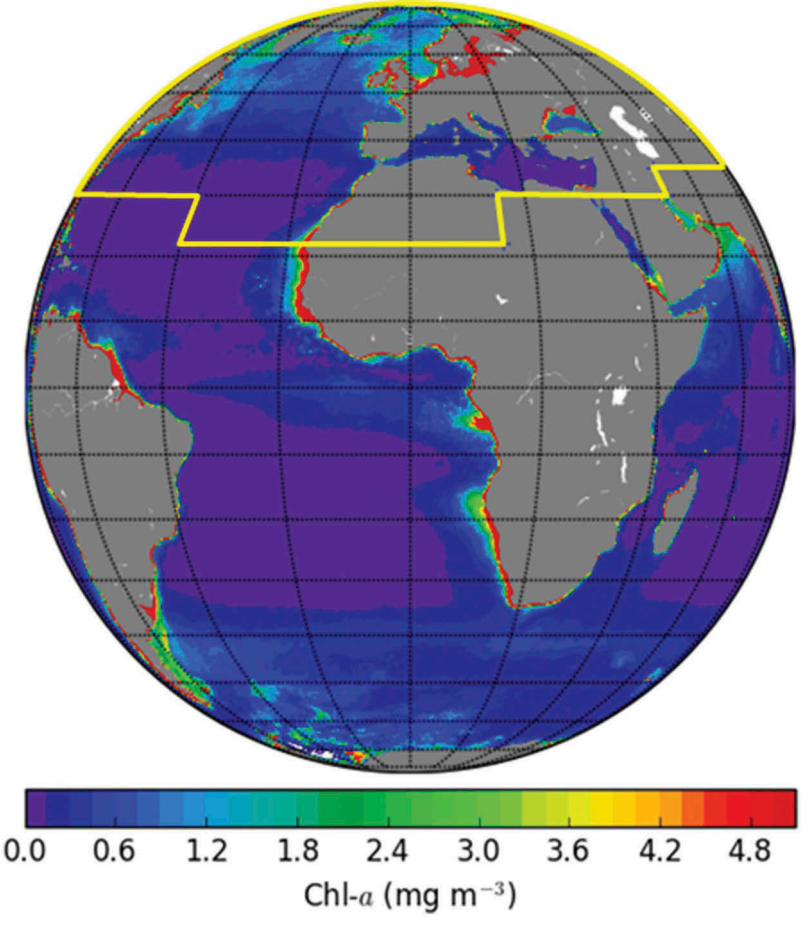

Figure 1. Position of the LAC zone (local area coverage) for MTG satellite (coordinates of the LAC zone is provided by from EUM/MTG/SPE/07/0036 2010). LAC zone could be scanned in RSS mode (one image every 2.5 min). Background represents MODIS chl-*a* climatology.

revisit period is 10 min for FDSS and 2.5 min for RSS. Similarly to AHI, FCI has also blue and green spectral bands (Vis0.4 and Vis0.5, see Table 1) which may allow to determine chl-*a* for open ocean clear waters (case 1 waters, Morel and Prieur 1977) from a blue-green band ratio algorithm (O'Reilly et al. 1998; Ruddick et al. 2014; Murakami 2016). Nevertheless, such marine applications for FCI need to be further investigated as the spectral and radiometric characteristics of FCI are far from the minimum requirements recommended for ocean colour sensors (IOCCG 2012b). Focusing on the region of the Gulf of Lion in the Mediterranean Sea, Peschoud et al. (2016) have showed that FCI data could be used to retrieve short-term variability of chl-*a* and SPM in coastal waters if they are merged with data from a Sun-synchronous ocean colour dedicated sensor. To further investigate FCI capabilities in marine domain, the present study aims to determine if FCI radiometric specificities, as given in the End-User Requirement Document (EUM/MTG/SPE/07/0036 2010), allow to compute chl-*a* with an acceptable noise-related uncertainty at relevant spatio-temporal scales.

Based on the spectral characteristics of the FCI sensor, a model applicable only to clear waters is proposed to obtain chl-*a* from remote-sensing reflectance (R_{rs}) of the Vis0.4 and Vis0.5 spectral bands. The impact of FCI noise is assessed by adding noise to R_{rs} measurements and calculating the corresponding error in retrieved chl-*a*. Tests are made by averaging FCI data in space and/or time to determine for which resolution low (less than 10%) noise-related error on chl-*a* can be obtained. The contribution of the atmospheric correction to radiometric noise is also assessed. Note however that questions about atmospheric correction performance, other than noise, are beyond the scope of this study. A simple atmospheric correction algorithm is proposed and supposed to be able to remove the true contribution from atmosphere to top-of-atmosphere (TOA) reflectance signal. This assumption is reasonable here since the present study focuses on clear waters where atmospheric correction is facilitated because of the strong water absorption in red and near-infrared (NIR) bands (Gordon and Wang 1994) and because FCI contains enough spectral bands in NIR and shortwave infrared (SWIR). Finally, a comparison is made between FCI and the minimum requirements for ocean colour sensors (IOCCG 2012b) and the potential domain of application of FCI data for chl-*a* is presented.

2. Methods

2.1. *Chl-a model*

FCI contains blue and green spectral bands: Vis0.4 and Vis0.5 centred on 0.444 µm and 0.510 µm, respectively. As in oligotrophic and mesotrophic waters, the blue over green ratio of remote-sensing marine reflectance (R_{rs}) is considered as a good indicator of chl-*a* (Morel and Prieur 1977; Bricaud, Morel, and Andre 1987; O'Reilly et al. 1998), a chl-*a* model based on the $R_{rs}{}^{0.444}$:$R_{rs}{}^{0.510}$ band ratio ($BR^{444:510}$ hereafter) is built with the National Aeronautics and Space Administration bio-Optical Marine Algorithm data set (NOMAD, Werdell and Bailey, 2005). First, data corresponding to case 1 waters were selected applying the methodology proposed by Lee and Hu (2006). A linear model relating the logarithm of chl-*a* to the logarithm of $BR^{444:510}$ was fitted to data (Figure 2(a)), Equation (1)). With a coefficient of determination (R^2) of 0.86 and a root mean square error (RMSE) of 0.21, this model is

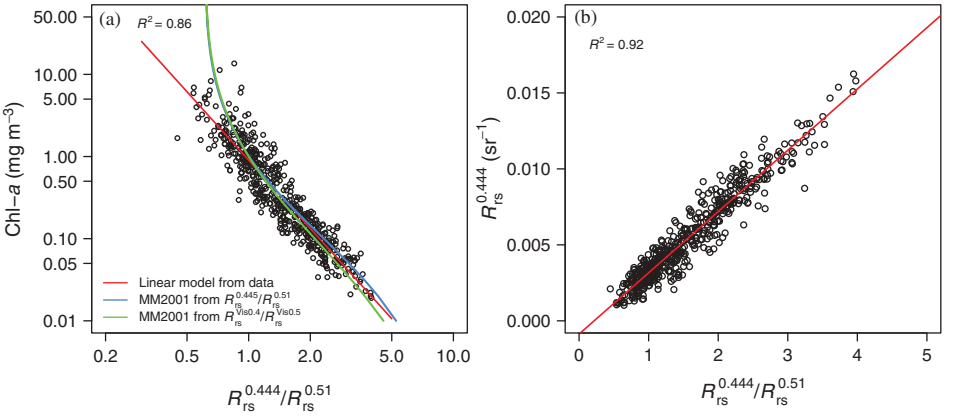

Figure 2. [left, panel a] Scatter plot of chl-*a* as a function of the $BR^{444:510}$ (=$R_{rs}{}^{0.444}$:$R_{rs}{}^{0.510}$). Both, chl-*a* and $BR^{444:510}$ are on log scale. The red line represents the linear model between log-chl-*a* and log-$BR^{444:510}$. Blue and green curves are outputs of Morel and Maritorena (2001) model. For the blue curve, band ratio was derived from reflectances at 445 and 510 nm whereas for the green curve, reflectances were integrated over 415–475 and 490–530 nm ranges to simulate FCI Vis0.4 and Vis0.5 bands. For high chl-*a* values, blue and green curves are superposed. [right, panel b] Scatter plot of $R_{rs}{}^{0.444}$ as a function of $BR^{444:510}$. The red line represents the linear model between two variables.

effective for determining chl-*a* for values ranging between 0.02 and 10.00 mg m^{-3}. For comparison, OC2V4 and OC4V4 algorithms (O'Reilly et al. 2000) present coefficients of determination of 0.88 and 0.89, respectively, and RMSE of 0.22 and 0.23. The simple prototype FCI algorithm is thus almost as accurate as standard chl-*a* algorithms. Although it could be refined before use in an operational processing system, it is certainly sufficient for the present proof-of-concept study.

$$\text{chl} - a = \exp\left(-0.101 - 2.762 \ln\left(\text{BR}^{444:510}\right)\right) \quad (1)$$

This model derived from the NOMAD data set does not take into account FCI bandwidth (see Table 1). This point is further dealt with in Section 4.1 and shows that the width of the FCI spectral bands does not significantly modify the relationship between chl-*a* and blue-green band ratio.

In case 1 waters, where bio-optical properties are essentially affected by phytoplankton and associated organic matter, the whole R_{rs} spectrum is controlled by chl-*a* so that a specific R_{rs} value is expected for a given chl-*a* value (Morel and Maritorena 2001; Gordon et al. 1988b). Hence, a second linear model was built from the NOMAD data set for case 1 waters between $BR^{444:510}$ band ratio and $R_{rs}{}^{0.444}$ (Figure 2(b), Equation (2)). From this model, a unique couple of $R_{rs}{}^{0.444}$ and $R_{rs}{}^{0.510}$ values is obtained for each value of $BR^{444:510}$ so that simulations can be made for a continuous range of R_{rs}.

$$R_{rs}^{0.444} = -0.00087 + 0.00403\text{BR}^{444:510} \quad (2)$$

In the following, when the error associated to a particular chl-*a* value is analysed, the corresponding $BR^{444:510}$ value is obtained with Equation (1) and the associated remote-

sensing reflectance (R_{rs} $^{0.444}$ and R_{rs} $^{0.510}$) or water leaving radiance values are derived from Equation (2).

2.2. *Radiometric noise*

The SNR is specified for each FCI band in the EURD document (2010; Table 1) for a reference radiance level (L_{ref}) where radiance is related to reflectance by

$$L = \frac{\alpha F_0}{\pi} = \frac{\rho^{TOA} \cos\theta_S F_0}{\pi} \tag{3}$$

where F_0 is the extraterrestrial solar irradiance and α is the TOA reflectance (ρ^{TOA}) multiplied by the cosine of the solar zenith angle ($\cos\theta_S$). In EURD (2010) document, for each band, reference signal-to-noise ratios (SNR_{ref}) are given for $\alpha = \alpha_{ref} = 0.01$ (see also Table 1). Because photonic noise is the most significant source of noise in the FCI instrument (Peschoud et al. 2016; EUM/MTG/SPE/07/0036 2010), to estimate SNR at radiance level L (α) different from L_{ref} (α_{ref}), the following scaling function (Equation (4)) must be applied.

$$SNR = (SNR)_{ref}\sqrt{\frac{\alpha}{\alpha_{ref}}} \tag{4}$$

Noise equivalent reflectance (ρ_{NE}) indicates the level of noise in reflectance units. It is the minimum variation of reflectance that the instrument can detect (Gibbons and Richard 1979). ρ_{NE} is also defined as the standard deviation of a homogeneous radiometric signal (EUM/MTG/SPE/07/0036 2010; Hu et al. 2012) and can be calculated in practice from satellite imagery as shown by Hu et al. (2012). ρ_{NE} is computed from Equation (5) where d is Sun–Earth distance in Astronomical Units.

$$\rho_{NE} = \frac{\pi \frac{L}{SNR} d^2}{F_0 \cos\theta_S} \tag{5}$$

Combining Equations (3) and (4) in Equation (5) and using the approximation $d = 1$, we obtain for ρ_{NE},

$$\rho_{NE} = \frac{\sqrt{\rho^{TOA}\alpha_{ref}}}{SNR_{ref}\sqrt{\cos\theta_S}} \tag{6}$$

Then, ρ_{NE} varies with TOA reflectance (ρ^{TOA}) and the solar zenith angle (θ_S). To estimate ρ^{TOA} under typical oceanic conditions, simulations were performed with the Py6S code for atmospheric radiative transfer (Wilson 2012). Simulations were made for eight locations in the North Atlantic Ocean and in the Mediterranean Sea (see map on Figure 3(a)), the 15th day of each month and every hour. The position of the SEVIRI sensor on MSG3 (i.e. equatorial plan, longitude = 0°) was used to represent the position of the FCI instrument and a maritime model was selected for simulating aerosols. The aerosol optical thickness at 550 nm was set at 0.1. Ground conditions were selected to simulate an oligotrophic ocean with chl-*a* concentration of 0.3 mg m^{-3} and no wind stress.

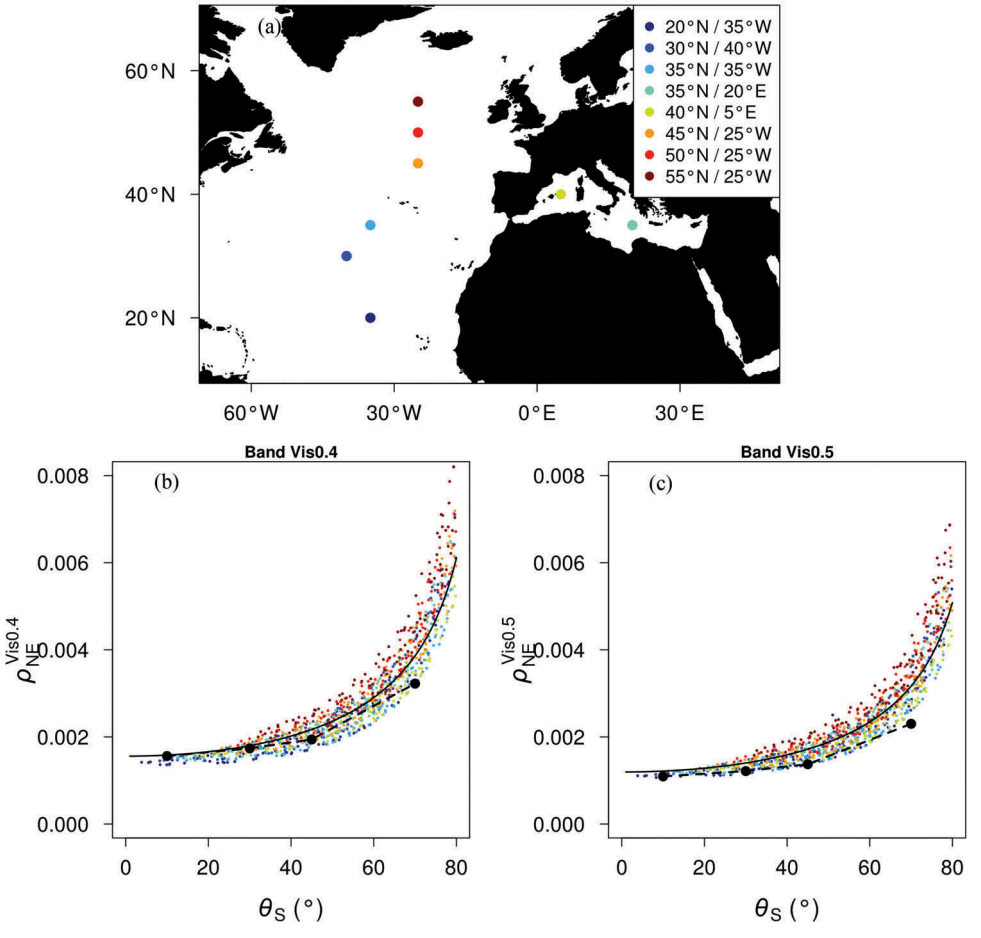

Figure 3. Relationship between ρ_{NE} and θ_S (solar zenith angle). Model defined in Equations (7(a) and 7(b)) are represented with the solid black lines for $\theta_V = 55°$. The ρ^{TOA} values used to determine ρ_{NE} (colours dots panels b and c) were simulated from the Py6S algorithm for atmospheric radiative transfer (see text for details) at eight different locations (panel a). Big black dots refer to the ρ_{NE} values obtained for the FCI noise specification but using MODIS typical TOA radiances over oligotrophic regions (Hu et al. 2012) instead of Py6S simulations.

As ρ_{NE} varies with ρ^{TOA} and θ_S (Equation (6)) and as Rayleigh reflectance that mainly depends on solar and view zenith angles (θ_S and θ_V, respectively; (Gordon, Brown, and Evan [1988a]) highly contributes to ρ^{TOA}, we attempted to express ρ_{NE} as a function of θ_S and θ_V only. To this end, linear regressions were computed between ρ_{NE} and the product of 1:√cos θ_S and 1:√cos θ_V,

$$\rho_{NE}^{Vis0.4} = -1.69.10^{-3} + 2.46.10^{-3} \frac{1}{\sqrt{\cos(\theta_S)}} \frac{1}{\sqrt{\cos(\theta_V)}} \quad (7a)$$

$$\rho_{NE}^{Vis0.5} = -1.58.10^{-3} + 2.10.10^{-3} \frac{1}{\sqrt{\cos(\theta_S)}} \frac{1}{\sqrt{\cos(\theta_V)}} \quad (7b)$$

With R^2 of 93.5% and 93.2%, respectively, linear regression models displayed in Equations (7(a)) and (7(b)) were found to be satisfactory to estimate ρ_{NE} over average oceanic and atmospheric conditions. An additional test showed that changing the aerosol properties does not strongly affect ρ_{NE}. Indeed, doubling the aerosol optical thickness at 550 nm results to an increase in ρ_{NE} by only 6% on average in each band.

Figure 3(b,c) show the ρ_{NE} variability as a function of θ_S only. Results display a clear increase of ρ_{NE} with θ_S which becomes particularly strong for θ_S values higher than 60° (ρ_{NE} values more than double for θ_S increasing from 60° to 80°). Py6S simulations (colour dots on Figure 3(b,c) are also in agreement with TOA radiances observed in MODIS bands 443 nm (panel b) and 531 nm (panel c) above oligotrophic ocean (Hu et al. 2012, big black dots). Finally, as ρ_{NE} is mostly affected by θ_S (see Figure 3), we decided to analyse only the impact of θ_S on noise-induced chl-*a* error and we set θ_V to 55° for the determination of ρ_{NE} (for the different locations displayed on Figure 3(a), θ_V ranges between 45° and 66°). The resulting models are displayed on Figure 3(b,c) with black solid lines.

2.3. *Analysis of noise*

Reflectance at TOA (ρ^{TOA}) measured by the sensor is the sum of atmospheric and oceanic contributions,

$$\rho^{TOA} = \rho_r^{TOA} + \rho_a^{TOA} + t_0 t_v \rho_w^{0+} \tag{8}$$

In Equation (8), ${\rho_r}^{TOA}$ and ${\rho_a}^{TOA}$ are the reflectances due to Rayleigh and aerosol scattering, respectively. ${\rho_w}^{o+}$ is the water leaving reflectance defined by Mobley (1994) and t_0 and t_v are the atmospheric transmittances for water leaving radiance from Sun to sensor and sensor to sea, respectively. However, the values measured by sensor and referred by $\rho^{TOA,N}$ (N indicates that noise is included) are not the 'true' values as an error ($\Delta\rho^{TOA}$) due to radiometric noise is added.

$$\rho^{TOA,N} = \rho^{TOA} + \Delta\rho^{TOA} \tag{9}$$

For simplification, we suppose to first order that $t_0 = t_v = 1$ (perfectly transparent atmosphere) and that the atmospheric correction process is perfect so that no additional error is introduced through this process. The validity of the last hypothesis is analysed in Section 3.3. With these assumptions, the estimation of the ${\rho_w}^{0+,N}$ derived from $\rho^{TOA,N}$ can be expressed as

$$\rho_w^{0+,N} = \rho_w^{0+} + \Delta\rho^{TOA} \tag{10}$$

From this point, two analyses are performed in parallel in this study (1) an analytic analysis of noise-induced error and (2) a simulation exercise based on a large number of samples.

2.3.1. *First-order Taylor series expansion*

Given that ${\rho_w}^{0+} = \pi . R_{rs}$, the standard deviation of noise-induced error on the band ratio $BR^{444:555}$ ($\Delta BR^{444:510}$), can be computed with the first-order Taylor series expansion assuming that noise in ${R_{rs}}^{0.444}$ and ${R_{rs}}^{0.510}$ are uncorrelated,

$$\Delta \mathrm{BR}^{444:510} = \left[\left(\frac{\partial BR^{444:510}}{\partial R_{\mathrm{rs}}^{0.444}} \Delta R_{\mathrm{rs}}^{0.444} \right)^2 + \left(\frac{\partial BR^{444:510}}{\partial R_{\mathrm{rs}}^{0.510}} \Delta R_{\mathrm{rs}}^{0.510} \right)^2 \right]^{1:2} \quad (11)$$

$$\text{with } \Delta R_{\mathrm{rs}}^{0.444} = \frac{1}{\pi} \Delta \rho_{0.444}^{\mathrm{TOA}} \text{ and } \Delta R_{\mathrm{rs}}^{0.510} = \frac{1}{\pi} \Delta \rho_{0.510}^{\mathrm{TOA}}.$$

Developing Equation (11) and replacing $\Delta\rho^{\mathrm{TOA}}$ by ρ_{NE}, the average noise level, we obtain

$$\Delta \mathrm{BR}^{444:510} = \left[\left(\frac{\rho_{\mathrm{NE}}^{\mathrm{Vis0.4}}}{\pi R_{\mathrm{rs}}^{0.510}} \right)^2 + \left(\frac{R_{\mathrm{rs}}^{0.444} \rho_{\mathrm{NE}}^{\mathrm{Vis0.5}}}{\pi \left(R_{\mathrm{rs}}^{0.510} \right)^2} \right)^2 \right]^{1:2} \quad (12)$$

$\Delta \mathrm{BR}^{444:510}$ was computed for a series of band ratio values ranging between 0.4 and 4.0 (chl-*a* ranging between 0.02 and 11.00 mg m^{-3}) and was introduced in Equation (1). The resulting chl-*a* value was then compared to the value obtained when $\Delta \mathrm{BR}^{444:510}$ is set to 0. The error on chl-*a* was finally measured as the absolute percentage difference (APD),

$$\mathrm{APD} = \frac{|\mathrm{chl}-a_{\mathrm{N}} - \mathrm{chl}-a_{\mathrm{r}}|}{\mathrm{chl}-a_{\mathrm{r}}} \quad (13)$$

where chl-a_{N} refers to the chl-*a* estimation including noise whereas chl-a_{r} is the reference (i.e. chl-*a* when no noise is introduced).

2.3.2. *Noise simulation exercises*

The first-order analytical approach of Section 2.3.1 is complemented with a large number of simulations allowing a more precise calculation of expected noise-induced chl-*a* errors. For each value of chl-*a* (associated to a unique couple of $R_{\mathrm{rs}}{}^{0.444}$ and $R_{\mathrm{rs}}{}^{0.510}$ values, see Equations (1) and (2)), 10,000 simulations were performed. For that purpose, it was assumed that $\Delta\rho^{\mathrm{TOA}}$ in Equation (10) is uniformly distributed in the interval $[-\sqrt{3}\rho_{\mathrm{NE}}; +\sqrt{3}\rho_{\mathrm{NE}}]$. In other words, it was assumed that $\Delta\rho^{\mathrm{TOA}}$ distribution is uniform with mean 0 and variance $\rho_{\mathrm{NE}}{}^2$. An additional test showed that replacing the Uniform distribution by a Gaussian distribution produces comparable results. Finally, for each simulation, the absolute percentage difference was computed (see Equation (13)).

3. Results

3.1. *Noise-related error on chl-a for a single pixel*

The noise level estimated with ρ_{NE} is compared on Figure 4 to water leaving reflectance signal ($\rho_{\mathrm{w}}{}^{0+}$) for different values of θ_{S}. For the blue band (Vis0.4), SNR ($\rho_{\mathrm{w}}{}^{0.444}$: $\rho_{\mathrm{NE}}{}^{0.444}$) increases when chl-*a* decreases. This trend is due to the inverse relationship between chl-*a* and $\mathrm{BR}^{444:510}$; high chl-*a* values are associated to low $R_{\mathrm{rs}}{}^{0.444}$ values which are then closer to the noise level ($\rho_{\mathrm{NE}}{}^{0.444}$). For low chl-*a* concentrations, $\rho_{\mathrm{w}}{}^{0.444}$: $\rho_{\mathrm{NE}}{}^{0.444}$ ranges between 10 and 30 depending on θ_{S} whereas it becomes critical for chl-*a* higher than 2 mg m^{-3}. A different pattern is observed for the green band (Vis0.5) where the $\rho_{\mathrm{w}}{}^{0.510}$: $\rho_{\mathrm{NE}}{}^{0.510}$ is almost constant for chl-*a* lower than 2 mg m^{-3} with values ranging between 3 and 8 depending on θ_{S}. This arises because $\rho_{\mathrm{w}}{}^{0.510}$ varies little with chl-*a*. Overall, SNR for ρ_{w} ($\Delta\rho_{\mathrm{w}}$:ρ_{w}) is much worse than SNR given for FCI instrument ($\Delta\rho^{\mathrm{TOA}}$:$\rho^{\mathrm{TOA}}$) because

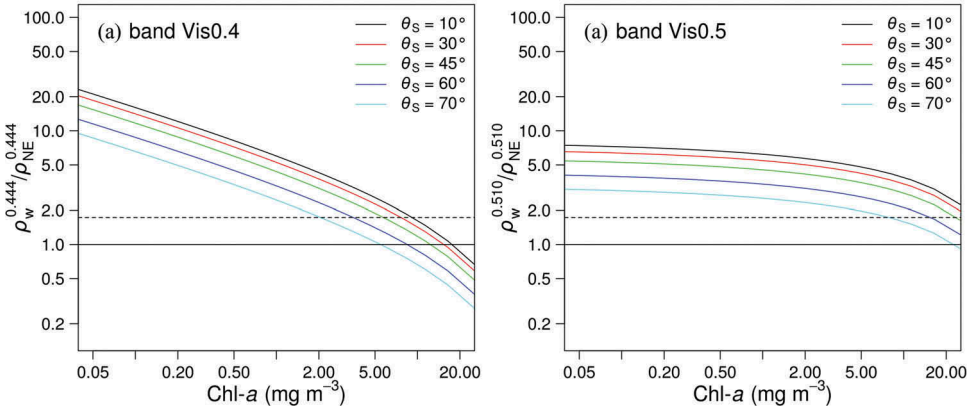

Figure 4. Variability of the ρ_w:ρ_{NE} ratio as a function of chl-*a* concentration for different values of solar zenith angle (θ_S). Horizontal dotted line refers to the limit ρ_w:$\rho_{NE} = \sqrt{3}$. Under this limit, the noise estimated from a uniform distribution with standard deviation ρ_{NE} can equal the signal level (ρ_w).

ρ_w is only a small fraction of ρ^{TOA} but, if noise associated to atmospheric correction is neglected, $\Delta\rho_w$ equals $\Delta\rho^{TOA}$ (=ρ_{NE} as average noise conditions are considered).

Both, theoretical error analysis and simulation exercises show relatively high error for chl-*a* when a single pixel is considered (Figure 5). On Figure 5(a), following the theoretical approach, an error estimation is calculated for each point representing case 1 waters in the NOMAD data set. Points display a significant scattering which is due to the variability of the $R_{rs}{}^{0.444}$ *versus* $BR^{444:510}$ relationship (Figure 2(b)). For a same value of $BR^{444:510}$, points with higher values for $R_{rs}{}^{0.510}$ and $R_{rs}{}^{0.444}$ are less impacted by noise and display smaller errors. On panels b and c, calculations are made for a continuous

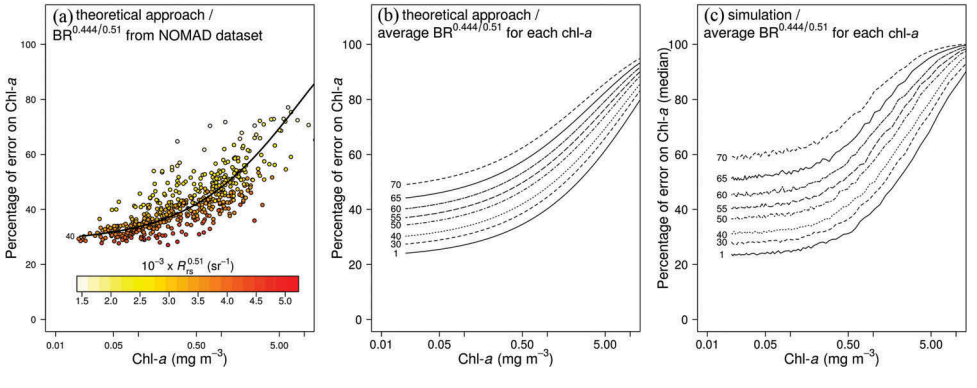

Figure 5. Noise-induced error on chl-*a* as a function of the chl-*a* concentration. The error is represented as the absolute percentage difference. On panel a, the error is computed with the theoretical approach for each data point of the NOMAD data set and the colour refers to the value of $R_{rs}{}^{510}$. In panels b and c, for each value of chl-*a*, the average value of $BR^{444:510}$ is retained (see Figure 2(b)), and the impact of the solar zenith angle on chl-*a* error is investigated. Solar zenith angles are indicated for each line. For the simulation exercise (panel c), the median absolute percentage difference is represented.

range of $BR^{444:510}$ values and using the statistical model developed for $R_{rs}{}^{0.444}$ (see Section 2.1). Results show that chl-*a* error is almost constant, at about 20–30%, for chl-*a* lower than 0.5 mg m^{-3} and moderate θ_S. Above this limit, error increases rapidly to reach 80–100% for chl-*a* = 10 mg m^{-3} whatever θ_S. θ_S has a major impact on chl-*a* error for low chl-*a* values. Indeed, at chl-*a* = 0.05 mg m^{-3}, error ranges between 20% (θ_S = 1°) and 60% (θ_S = 70°) according to the simulation exercise (Figure 5(c)). Globally, theory and simulation graphics are in agreement for θ_S lower than 60°. For higher angles and especially at low chl-*a* concentration, error is underestimated in the theoretical analysis (panel b) compared to the simulation exercise (panel c) because when θ_S is high, the error on water leaving reflectance is so large that the first-order Taylor approximation is no longer applicable.

To summarise, the analysis of error on chl-*a* for a single pixel reveals high noise-induced errors. In the most favourable situation, median error is about 20%. Error is even higher for high chl-*a* values and high θ_S values. Although for θ_S lower than 60°, error is contained in a comparatively small range, it increases rapidly for θ_S higher than 60°. Hence, estimating chl-*a* from FCI for solar zenith angles higher than 60° should be very difficult. As also revealed by Figure 4, high chl-*a* values display high relative error. To solve this problem, one option is to average water leaving reflectance data for several pixels close in time and/or space in order to reduce noise level on chl-*a*.

3.2. *Noise-related error on chl-a for several spatially/temporally averaged pixels*

Assuming that chl-*a* is almost constant over small temporal and spatial ranges, single pixels can be averaged to reduce noise and final error on chl-*a*. To determine what could be the best compromise between the spatio-temporal resolution and error on chl-*a*, different scenarios were tested. These scenarios comprise a spatial averaging (9 pixels averaged, giving spatial resolution of 3 km instead of 1 km) and/or a temporal averaging (data averaged over 1 h to keep diurnal variability). Degrading temporal resolution to 1 h allows to average 6 data points in FDSS mode (one image every 10 min) and 24 data points in the RSS mode (one image every 2.5 min). Scenarios were tested through the simulation exercise by averaging n estimations of $\Delta\rho^{TOA}$ (n is number of pixels averaged). Although this study only focuses on one spatial (i.e. 3 km) and one temporal (1 h) resolution, resulting in five different averaging scenarios (1 h FDSS, 1 h RSS, 3 km, 1 h FDSS/3 km, and 1 h RSS/3 km), one can easily foresee results for other resolutions considering the number of pixels averaged. For instance, reducing the spatial resolution to 5 and 7 km gives averages of 25 and 49 pixels, respectively, which is close to the 1 h RSS (24 pixels averaged) and 1 h FDSS/3 km (54 pixels averaged) scenarios.

On Figure 6, three scenarios are tested: the reference scenario with no averaging (a single pixel is considered, solid line), only spatial averaging (9 pixels averaged, dashed line), and spatial and temporal averaging in case of the FDSS mode (9 × 6 pixels averaged, broken line). Results clearly show that the more the resolution is reduced, the better is the chl-*a* distribution curve and the narrower is the dispersion around the average (Table 2). Without any averaging process, the chl-*a* distribution is relatively flat, especially for high chl-*a* value (2 mg m^{-3}, red curve), which prevents any satisfactory estimation of the chl-*a*. Indeed, for chl-*a* = 2 mg m^{-3}, the standard deviation of the distribution is 4.32 mg m^{-3} and the median absolute error is 63.2% (Table 2). However,

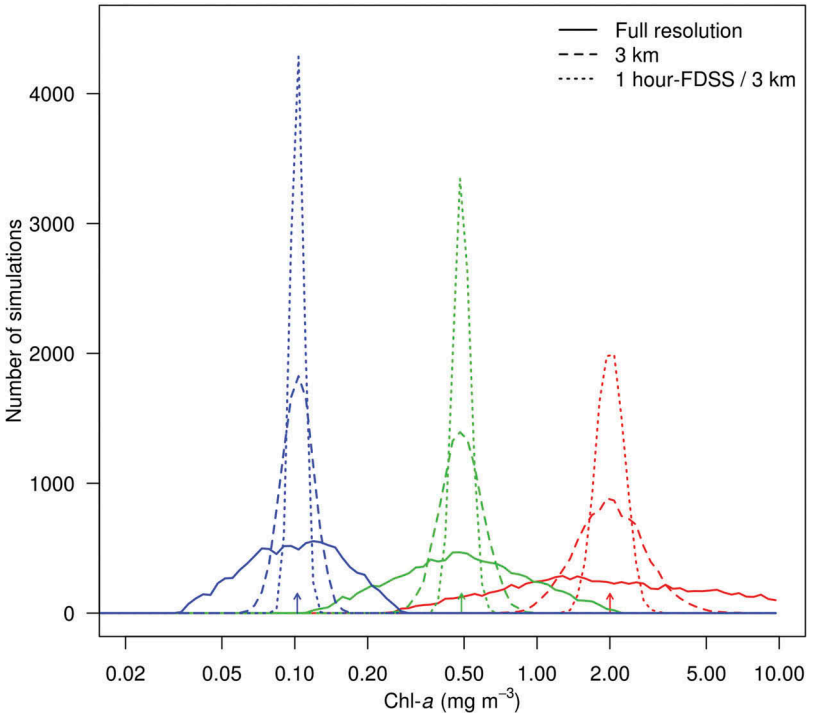

Figure 6. Frequency distribution curves of the chl-*a* estimations. Three values of chl-*a*: 0.1, 0.5, and 2.0 mg m^{-3} were simulated (blue, green, and red, respectively) for $\theta_S = 40°$. For each of them, different averaging processes were tested: full resolution (1 pixel averaged), 3 km (9 pixels averaged), and 1 h in FDSS mode with 3 km (9 × 6 pixels averaged). The averaging process is applied to water leaving reflectances. In each case, 10,000 simulations were produced. The standard deviation and the median absolute percentage difference of each distribution are given in Table 2.

Table 2. Standard deviation (SD) and median absolute percentage difference (MAPD) on chl-*a* estimations after introduction of noise (10,000 simulations) for the chl-*a* values and the spatio-temporal resolutions tested on Figure 6.

	Number of pixels averaged					
	1 pixel		9 pixels		9 × 6 pixels	
chl-*a* (mg m^{-3})	SD (mg m^{-3})	MADP (%)	SD (mg m^{-3})	MADP (%)	SD (mg m^{-3})	MAPD (%)
2	4.32	63.2	0.73	21.3	0.26	8.7
0.5	0.36	40.9	0.10	13.5	0.04	5.6
0.1	0.05	32.1	0.02	10.2	0.006	4.2

Standard deviations are expressed in mg m^{-3}.

when pixels are spatially and temporally averaged (54 pixels averaged), dispersion and error are strongly reduced (MAPD ranges between 4% and 9%, see Table 2) permitting an acceptable estimation for chl-*a*. Previous results are confirmed by Figure 7 which is the same as Figure 5(c) but shows the error curves for each scenario at $\theta_S = 30°$ (panel a) and $\theta_S = 60°$ (panel b). To obtain an estimation of chl-*a* with an error inferior to 10% for chl-*a* concentrations up to 1 mg m^{-3}, temporal and spatial averaging are necessary (i.e. 1 h–3 km FDSS mode or 1 h–3 km RSS mode). The RSS mode (one scan every 2.5 min)

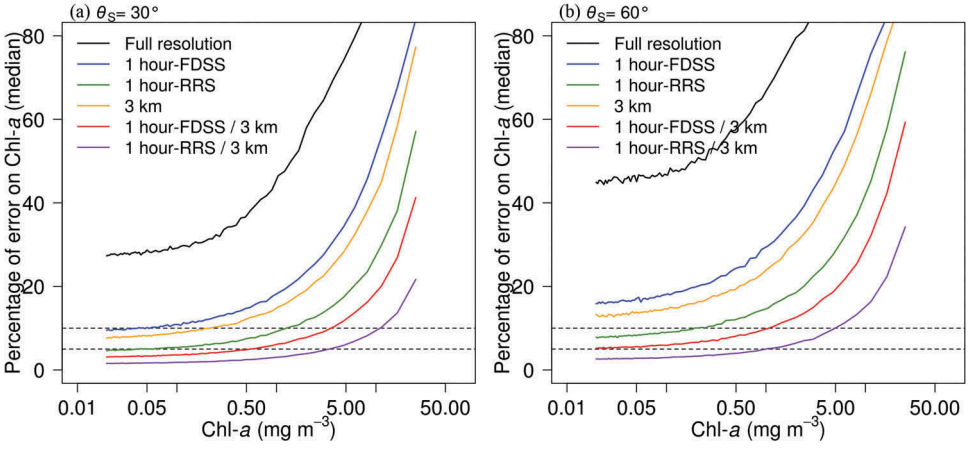

Figure 7. Error on chl-*a* as a function of the chl-*a* concentration for different averaging scenarios (see text for details) at $\theta_S = 30°$ (panel a) and $\theta_S = 60°$ (panel b). Black dotted lines represent the 5% and 10% error limits.

that covers the northern part of the disk will be very useful for the subpolar North-Atlantic. Indeed, the high number of data available balances high θ_S values and high chl-*a* concentrations observed during spring bloom in this region. At lower latitudes, where oligotrophy prevails, chl-*a* is generally low and less averaging, e.g. only spatial (9 pixels averaged) or only temporal (6 pixels averaged) can be considered for observations achieved around noon (small θ_S).

3.3. *Impact of atmospheric correction on chl-a final error*

In the previous sections, additional error due to the atmospheric correction process was supposed to be negligible compared to the error associated to ρ^{TOA} in Vis0.4 and Vis0.5 bands. This assumption which is based on the radiometric specificities of the MTG/FCI sensor (i.e. high radiometric noise in Vis bands compared to NIR and SWIR bands) is analysed here. According to the Equation (8), ${\rho_w}^{0+}$ depends on ρ^{TOA} but also on ${\rho_r}^{TOA}$, ${\rho_a}^{TOA}$, and on $t_0 t_v$. ${\rho_r}^{TOA}$ and $t_0 t_v$ are computed from Sun/viewing geometry and they have no noise-related uncertainty. However, noise may affect calculation of ${\rho_a}^{TOA}$, the aerosol contribution to total TOA reflectance (Hu, Carder, and Muller-Karger 2001). Then, ${\Delta\rho_w}^{0+}$ contains two noise-related components,

$$\Delta\rho_w^{0+,i} = \frac{1}{t_v^i t_0^i}\left(\Delta\rho^{TOA,i} + \Delta\rho_a^{TOA,i}\right) \tag{14}$$

where i refers to the spectral band and ${\Delta\rho_a}^{TOA,i}$ is the error associated to TOA aerosol reflectance in band i.

To retrieve ${\rho_a}^{TOA}$ in bands Vis0.4 and Vis0.5, we propose to use FCI bands NIR0.8 and SWIR1.6 centred on 0.865 and 1.610 µm, respectively, because (1) these bands are not impacted by water vapour absorption in the atmosphere, conversely to bands NIR0.9 and SWIR1.3, and because (2) in clear waters, ${\rho_w}^{0+}$ can assume to be 0 in these bands

(Gordon and Wang 1994). Then, $\varepsilon = {\rho_a}^{NIR0.8}:{\rho_a}^{SWIR1.6}$ can be easily derived from ρ^{TOA} (note that the TOA superscript in Equation (8) has been dropped for simplification). In a processor, the aerosol reflectance can be extrapolated from NIR/SWIR to shorter wavelengths using tabulated aerosol models (Gordon and Wang 1994). For the present theoretical error analysis, the aerosol reflectance spectral variation is approximated by a power law 'Angstrom' model.

$$\rho_a^{Vis0.4} = \rho_a^{SWIR1.6}\left(\frac{444}{1610}\right)^{-A} \text{with } A = \frac{\ln(\varepsilon)}{\ln\left(1610/865\right)} \tag{15}$$

Then, uncertainty on ${\rho_a}^{Vis0.4}$ ($\Delta{\rho_a}^{Vis0.4}$) is the combination of the uncertainty on ${\rho_a}^{SWIR1.6}$ and on A (or ε).

To reduce noise on ε, a large spatial smoothing can be applied (Wang, Shi, and Jiang 2012) or a unique ε can be computed for a whole subscene (Neukermans et al. 2009; Vanhellemont and Ruddick 2015) because the horizontal length scale for variability of aerosol type is generally large. In such a situation, noise-related error on ε is negligible although areas with natural variability of aerosol type (e.g. atmospheric fronts) will be less well represented.

To test the impact of atmospheric correction on ${\rho_w}^{Vis0.4}$ uncertainty, different models of atmospheric correction have been tested with the following parametrisation: $\theta_S = 40°$, $\varepsilon = 1.4$, and ${\rho_a}^{SWIR} = 0.01$. In model 1, atmospheric correction is applied on a 1 pixel basis for the determination of ε and ${\rho_a}^{SWIR1.6}$. In model 2 and model 3, uncertainty on ε is reduced by averaging 9 and 81 pixels, respectively. In model 4, it is assumed that ε is free of noise. Finally, in model 5, the atmospheric correction process is assumed to be noise free and the only source of noise on ${\rho_w}^{Vis0.4}$ comes from $\rho^{TOA,Vis0.4}$. Frequency distribution curves for each model are displayed on Figure 8(a) and uncertainty budgets are provided in Table 3. Comparing model 1 (atmospheric correction applied on 1 pixel basis) and model 5 (no noise-related error in atmospheric correction), it clearly appears that atmospheric correction increases noise in ${\rho_w}^{Vis0.4}$. However, as soon as ε is averaged over a few pixels (i.e. 9 pixels), the frequency distribution curves are much narrower and are relatively close to the curve representing the model 5 (no noise-related error in atmospheric correction). Results also showed that averaging ε over a box of 9×9 pixels removes almost all ε uncertainty as curves from model 3 and model 4 are almost superimposed. Comparing model 4 (atmospheric correction error is only related to ${\rho_a}^{SWIR1.6}$) and model 5 (no error in atmospheric correction), the probability that error be in the $\pm\sqrt{3}({\rho_{NE}}^{Vis0.4} - \Delta{\rho_a}^{Vis0.4})$ interval (i.e. $\pm 1.3 \times 10^{-3}$) is the same in each curve. That represents about 50% of simulations. Outside this limit, introducing error due to the estimation of aerosol has a positive impact on error in the interval $[\sqrt{3}({\rho_{NE}}^{Vis0.4} - \Delta{\rho_a}^{Vis0.4}), \sqrt{3}({\rho_{NE}}^{Vis0.4})]$ (the same for the negative side) because a combination of positive $\Delta{\rho_a}^{Vis0.4}$ and negative $\Delta\rho^{TOA,Vis0.4}$, and *vice versa*, tends to reduce error. However, errors can also be accumulated which explains the expansion of the minimal–maximal error interval.

Uncertainty on ${\rho_a}^{Vis0.4}$ is of the same order of magnitude as uncertainty on $\rho^{TOA,Vis0.4}$ in model 1 and about 2.0–2.5 times lower in models 2, 3, and 4 (Table 3). It results that even if $\Delta{\rho_w}^{Vis0.4}$ increases from model 1 to model 5, the additional uncertainty from atmospheric correction is reduced as soon as ε is averaged over a few pixels. Indeed,

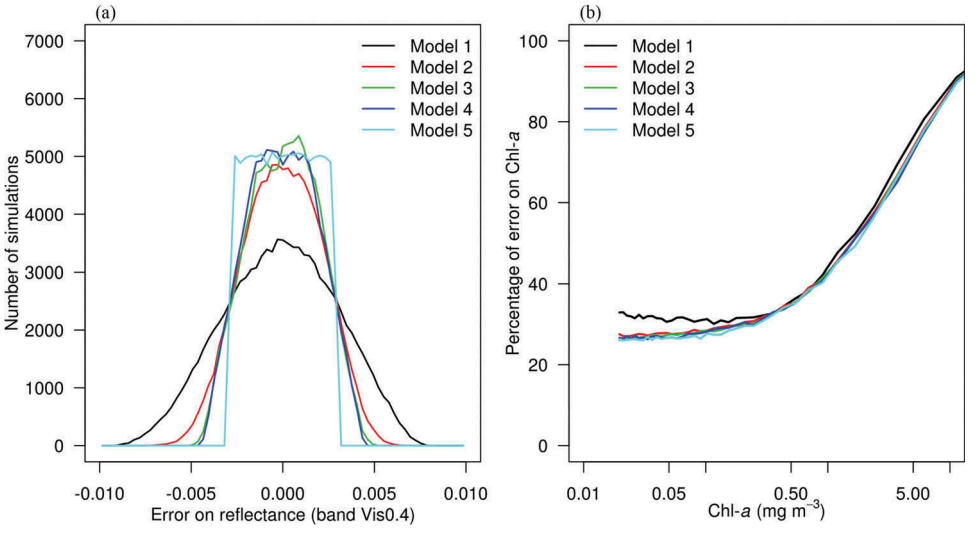

Figure 8. Left panel: Frequency distribution curve of errors added to $\rho_w^{Vis0.4}$ ($\Delta\rho_w^{Vis0.4}$) for different atmospheric correction models (see text Section 3.3 for details). Simulations were made with $\varepsilon = 1.4$ and $\rho_a^{SWIR1.6} = 0.01$. Right panel: The same as Figure 5(c) for simulations accounting (models 1–4) and not accounting (model 5) for the contribution of atmospheric correction to noise.

Table 3. Uncertainty on $\rho_a^{Vis0.4}$, $\rho^{TOA,Vis0.4}$, and $\rho_w^{Vis0.4}$.

	$\Delta\rho_a^{Vis0.4}$	$\Delta\rho^{TOA,Vis0.4}$	$\Delta\rho_w^{Vis0.4}$
Model 1	1.76×10^{-3}	1.63×10^{-3}	3.07×10^{-3}
Model 2	9.49×10^{-4}	1.68×10^{-3}	2.13×10^{-3}
Model 3	6.83×10^{-4}	1.68×10^{-3}	1.91×10^{-3}
Model 4	6.42×10^{-4}	1.68×10^{-3}	1.89×10^{-3}
Model 5	0	1.68×10^{-3}	1.68×10^{-3}

For five different atmospheric correction models, see Section 3.3 for a complete description. Uncertainty values have been computed from simulations containing in each case 100.000 samples.

compared to $\Delta\rho_w^{Vis0.4}$ in model 5, $\Delta\rho_w^{Vis0.4}$ increases by only 13% and 14% in model 4 and model 3, respectively. In consequence, almost no differences are observed between models 2, 3, and 4 and model 5 when the median absolute percentage difference on chl-*a* is analysed (Figure 8, panel b). This confirms the validity of previous results based on the assumption that the atmospheric correction process does not significantly affect the noise-related error on chl-*a*.

In opposition to previous studies which focus on ocean colour sensors (Jolivet et al. 2007; Hu, Feng, and Lee 2013), we demonstrated that noise-related uncertainty derived from atmospheric correction is less important than the direct effect of noise associated to TOA measurements in the visible range. This FCI specificity can be explained by the application of a dedicated atmospheric correction algorithm and by the radiometric performance of the FCI sensor which is far from that of typical ocean colour sensors. On one hand, whereas most of the atmospheric correction algorithms are based on Gordon and Wang (1994) and are applied on a 1 pixel basis, here it is proposed to average several pixels (e.g. 9 × 9) to compute ε which reduces uncertainty by a factor 2.5. Hence,

it is assumed that aerosol type varies over longer spatial scales than aerosol concentration (e.g. 9 km for aerosol type against 1 km for aerosol concentration). On the other hand, most of sensors dedicated to ocean colour application have very high radiometric performance in visible bands about 10 times higher than FCI performance (e.g. for SeaWiFS SNR@445nm = 950).

4. Discussion

4.1. *FCI characteristics compared to minimum requirements for ocean colour sensors*

The FCI instrument is designed for meteorological applications and its characteristics do not reach the minimum requirements for ocean colour sensors set by IOCCG 2012b. Nevertheless, the above results suggest that with some adaptations (i.e. specific band ratio chl-*a* algorithm, spatio-temporal averaging of data), chl-*a* could be retrieved from this sensor over open oceans. The (IOCCG 2012b) report suggests that a minimum SNR ratio at typical TOA radiances received by the sensor (i.e. 70.2 W m^{-2} μm^{-1} at 0.443 µm and 45.8 W m^{-2} μm^{-1} at 0.510 µm) should be 1000. Applied to the above typical TOA radiances with Equation (4), SNR is about 85 and 69 for FCI bands Vis0.4 and Vis0.5, respectively. FCI radiometric resolution is then more than 10 times lower than recommendations. That explains the necessity to average several pixels data to improve SNR. As SNR increases with square root of *n* (*n* being the number of pixels averaged), about 140 and 210 pixels should be averaged so that SNR reaches 1000 (minimum requirement for ocean colour sensor), which matches with the scenario 1 h–3 km in RSS mode that we recommend for bloom periods and mid-to-high latitude regions.

IOCCG (2012b) indicates also that satellite sensors should cover, without saturating, a preset range of TOA radiances representing all the radiances that a satellite sensor may observe during its mission. According to EURD document (2010), this last requirement is fully satisfied by FCI sensor as FCI dynamic ranges in Vis0.4 and Vis0.5 bands are wide (from 1% to 120% of F_0) and largely cover the minimum/maximum radiance mentioned by IOCCG (2012b).

Regarding spectral specifications, FCI Vis0.4 band is centred on the chl-*a* absorption peak which is commonly used in band ratio-based chl-*a* algorithms (O'Reilly et al. 1998). For normalisation, a spectral band centred on 0.555 µm and insensitive to chl-*a* is often used and the 0.510 µm band is rather utilised to replace the 0.444 µm band in case of high chl-*a*. Figure 2(a) shows that although it is not common and not suitable for very high chl-*a*, the $R_{rs}{}^{0.444}$: $R_{rs}{}^{0.510}$ band ratio can be used to derive chl-*a* for concentrations up to 10 mg m^{-3}.

Another difference between FCI and dedicated ocean colour sensors is the spectral resolution. Bandwidths for FCI bands Vis0.4 and Vis0.5 are, respectively, 60 and 40 nm whereas IOCCG (2012b) recommends a Full Width Half Maximum of 15 nm. To assess the impact of large FCI bands on the chl-*a*/band-ratio relationship, the Morel and Maritorena (2001) model for case 1 waters was used. R_{rs} spectra were modelled for various chl-*a* concentrations. Then, the chl-*a* *versus* $R_{rs}{}^{0.444}$:$R_{rs}{}^{0.510}$ relationship was built without any integration on R_{rs} (dark blue line Figure 2(a)) and with integration over the Vis0.4 and Vis0.5 bands (from 0.415 to 0.475 µm for the Vis0.4 and from 0.490 to 0.530 µm for

Vis0.5). Results (Figure 2(a)) display very little differences between the two curves. Curves deviate for low chl-*a* concentrations (chl-*a* lower than 0.5 mg m^{-3}) but the difference remains smaller than natural variability. In conclusion, the algorithm developed from the NOMAD data set should be suitable for the large FCI spectral bands, although a specific algorithm directly based on matchups between *in situ* chl-*a* and *in situ* ρ_w measurements representing FCI bands could be developed. In fact, the IOCCG (2012b) report recommends numerous and narrow bands to be able to derive additional information about aquatic bio-optical properties such as phytoplankton groups or colour dissolved organic matter absorption and to process both clear and turbid waters. Here, it is clear that spectral characteristics of FCI only permit the retrieval of chl-*a* in clear waters, but this does become possible at an hourly rather than daily temporal resolution.

Another requirement for typical ocean colour sensor is a good radiometric stability allowing to produce long-term (about 10 years) and consistent time-series for climatological studies and synoptic applications. FCI sensor is equipped with an in-flight calibration system based on solar light to guaranty the sensor stability (over the sensor time-life radiometric stability is expected to be less than 2%; EURD document, 2010). In addition, lunar calibration is planned to monitor relative sensor drift up to 0.9 µm. Finally, the MTG programme consists of four overlapping missions with an expected time-life of 8 years from 2019 to 2039. This design must permit cross-validation and the production of long-term time-series.

4.2. *Domains of application*

According to previous results, it seems difficult to estimate chl-*a* for solar zenith angles higher than 60° as after this limit ρ_{NE} increases rapidly (Figure 3). Despite this limitation, a large range of oceanic regions could be analysed with FCI data. Chl-*a* could be assessed year round between 40° S and 40° N (Figure 9) and between 30° S and 30° N, at least 4 h of data will available per day. In mid-latitudes (i.e. 40°–60°), estimations of chl-*a* should be available for more than half a year and in high latitudes (60°–80°), only the summer period will be accessible. As in the Atlantic Ocean, bloom timing shifts from winter to summer with latitude (Racault et al. 2012), the present limitation will not prevent the analysis of rapid chl-*a* variability during the productive season.

Another limitation following from this analysis is the difficulty to retrieve high chl-*a* values with the FCI bandset and SNR. Nevertheless, in open ocean, very high chl-*a* (i.e. chl-*a* > 5 mg m^{-3}) are not so frequent (Gregg and Casey 2004). For instance, the highest bloom amplitudes are observed along the North-West Atlantic shelf and reach about 2–3 mg m^{-3} (Devred, Sathyendranath, and Platt 2007; Racault et al. 2012; SeaWiFS climatology). Hence, although in regions observed by FCI (i.e. Atlantic Ocean and Mediterranean Sea), it is not impossible that chl-*a* value reach the upper limit of the FCI sensor (i.e. 5 mg m^{-3}), these events should be rare.

For a better appreciation of the potential of the FCI data in the subpolar North Atlantic, Figure 10 represents at point 55° N 25° W in the North Atlantic, the annual variability of chl-*a* for year 2014 as well as the 50% and 90% interval error considering FCI radiometric characteristics. Simulations were performed with the 3 km–1 h RSS averaging scenario and considering that 50% of data are not available because of

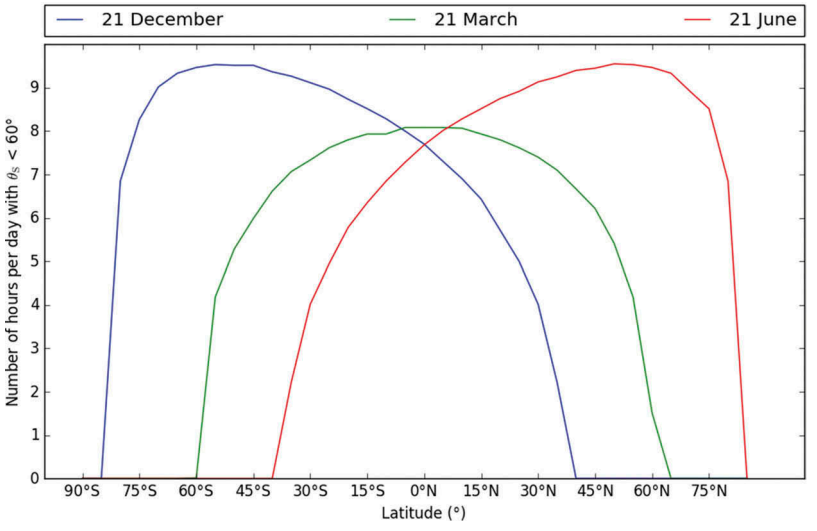

Figure 9. Number of hours per day when solar zenith angle is lower than 60° as a function of latitude and date.

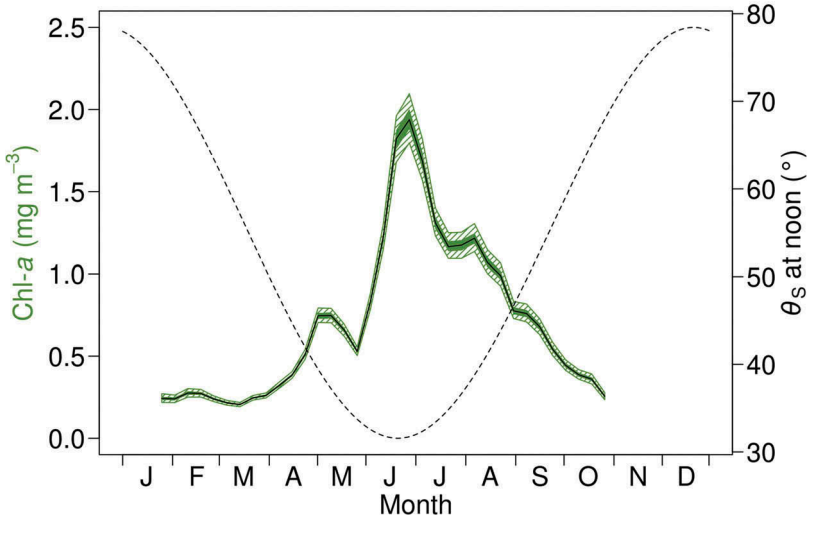

Figure 10. Chl-*a* during year 2014 at point 55° N 25° W (black solid line, MODIS Aqua data, 25 pixels averaged, filtered time-series with a 3-point running average). For each chl-*a* value, error intervals associated to FCI noise were computed at solar noon considering a 3 km/1 h scenario in RSS mode and a cloud coverage of 50%. Hatched and filled intervals represent the position of 90% and 50% of simulated points, respectively. Black dotted line shows θ_S at noon.

cloud coverage. Results show that the noise-induced error interval is much smaller than the amplitude of the chl-*a* annual cycle suggesting that seasonal variability of chl-*a* could be studied with chl-*a* estimations derived from FCI. Geo chl-*a* data should significantly contribute to our understanding of phytoplankton phenology which is currently biased because of cloud-related data gaps. Indeed, with Sun synchronous

Table 4. chl-*a* intervals containing 90% of simulated chl-*a* estimations for different values of chl-*a* and θ_S.

	θ_S = 30°		θ_S = 60°	
chl-*a* (mg m^{-3})	FDSS	RSS	FDSS	RSS
0.05	0.046–0.054	0.048–0.052	0.044–0.057	0.047–0.053
0.05 × 1.5	0.069–0.082	0.072–0.078	0.065–0.086	0.070–0.080
0.1	0.092–0.109	0.096–0.104	0.086–0.116	0.093–0.107
0.1 × 1.5	0.137–0.164	0.143–0.157	0.128–0.175	0.139–0.162
0.5	0.444–0.563	0.471–0.531	0.411–0.608[a]	0.453–0.551
0.5 × 1.5	0.656–0.858	0.702–0.802	0.603–0.936[a]	0.672–0.837
1	0.864–1.159	0.930–1.076	0.787–1.275[a]	0.887–1.128
1 × 1.5	1.270–1.783	1.379–1.633	1.142–1.990[a]	1.306–1.752

[a]Indicates conditions for which chl-*a* and 1.5 × chl-*a* intervals overlap.
chl-*a* interval is given for a value of chl-*a* as well as the same value multiplied by 1.5 (×1.5). Simulations were performed with the configuration 3 km–1 h in the FDSS and RSS modes (see text for details).
FDSS: Full Disc Scanning Service; RSS: Rapid Scan Service.

orbiting sensors, Cole et al., (2012) showed that about 50% of data are lacking in 8 days resolution time-series in the subpolar North Atlantic (about 50° N), resulting in an uncertainty of 25 and 10 days in the determination of bloom initiation date and bloom peak, respectively.

Pahlevan et al. (2013) consider that to capture chl-*a* diel variability, a 50% increase in chl-*a* must not be hidden by the radiometric noise of the Geo sensor. To test FCI radiometric performances regarding diurnal variability, 90% error intervals were computed in the configuration 1 h–3 km in FDSS and RSS modes for different values of chl-*a* and for these values multiplied by 1.5 (Table 4). Results showed that for low solar zenith angles and chl-*a* ranging between 0.05 and 1.00 mg m^{-3}, FDSS and RSS modes clearly distinguish baseline chl-*a* and upper chl-*a*. However, at high solar zenith angle (θ_S = 60°), the 3 km/1 h-FDSS averaging scenario is not sufficient to capture diurnal variability when chl-*a* exceeds 0.5 mg m^{-3} (lower and upper intervals overlap). In such conditions, it is necessary to enlarge the spatial averaging grid (i.e. 5 km × 5 km boxes for instance) or to use data from the RSS mode if available. Nevertheless, this test confirms that if diurnal chl-*a* variability is significant (i.e. 50% increase during the day), an appropriate averaging process allows to observe diurnal variability at 1 h temporal resolution.

5. Conclusion

Recent studies demonstrated that meteorological Geo sensors can be used for certain marine applications (Neukermans et al. 2009; Neukermans, Ruddick, and Greenwood 2012; Vanhellemont, Neukermans, and Ruddick 2014; Peschoud et al. 2016; Murakami 2016) and help to mitigate the absence of ocean colour Geo sensors. The present study aims to determine to which extent the low radiometric performances of the future FCI-sensor on-board MTG prevent an accurate retrieval of chl-*a* concentration in clear waters and how pixels should be spatio-temporally averaged to obtain chl-*a* estimations with an acceptable noise-related error. Hence, this study focuses only on noise-related error which is a major issue for the FCI sensor. However, other sources of uncertainty exist, as for example instrument artefacts, calibration errors, or imperfect bio-optical algorithm, and may degrade chl-*a* retrieval. These sources of error are not considered here and the reader should be aware that performances on chl-*a* presented in this study do not

represent the final expected accuracy of chl-*a* derived from FCI sensor but rather their upper limit. Result showed that the FCI sensor has sufficient radiometric specification to derive chl-*a* with an acceptable noise-related uncertainty in clear waters at 1 h and 3 km resolution. Indeed, taking advantage of the high acquisition rate of the FCI sensor (10 min FDSS mode or 2.5 min RSS mode), a 10% noise-related error on chl-*a* can be achieved if spatio-temporal resolution is degraded to 3 km and 1 h. The very high frequency acquisition mode (RSS mode) available for the northern hemisphere (latitude higher than 30° N) will be necessary to properly assess the spring bloom in the subpolar North-Atlantic and to assess diurnal variability when chl-*a* and θ_S are high (see Figure 1, yellow area). At low latitudes, the 10 min acquisition frequency available in the FDSS mode should be suitable given the low chl-*a* concentrations observed in this region (Figure1). Analysis also showed that the atmospheric correction process has only a small impact on chl-*a* retrieval, provided that aerosol type can be assumed constant over a subscene, as absolute FCI noise in the SWIR spectral bands is much smaller than noise in blue and green bands. Therefore, in a near future, we can expect to complement, thanks to the FCI sensor, chl-*a* information provided by Sun-synchronous ocean colour sensors. Indeed, high temporal resolution chl-*a* time-series should be available over large regions of the Atlantic Ocean and the Mediterranean Sea.

Acknowledgements

This study is part of the HIGHROC project funded by the European Community's Seventh Framework Programme (FP7/2007–2013) under grant agreement number 606797. NASA is thanked for providing MODIS AQUA data and the NOMAD data set. NOMAD data were contributed by participants in the NASA SIMBIOS Program (NRA-96-MTPE-04 and NRA-99-OES-09) and by voluntary contributors. We also gratefully thank Sandrine Mathieu (Thales Alenia Space) and Youva Aoun (Mines ParisTech) for providing detailed information on FCI radiometric noise. Two anonymous reviewers are thanks for their constructive comments on a first draft of the manuscript.

Disclosure statement

No potential conflict of interest was reported by the authors.

Funding

This study is part of the HIGHROC project funded by the European Community's Seventh Framework Programme (FP7/2007–2013) under grant agreement number 606797.

References

Bricaud, A., A. Morel, and J. Andre. 1987. "Spatial/Temporal Variability of Algal Biomass and Potential Productivity in the Mauritanian Upwelling Zone, as Estimated from CZCS Data." *Advances in Space Research* 7: 53–62. doi:10.1016/0273-1177(87)90164-5.

Cole, H., S. Henson, A. Martin, and A. Yool. 2012. "Mind the Gap: The Impact of Missing Data on the Calculation of Phytoplankton Phenology Metrics." *Journal of Geophysical Research: Oceans* 117.

Devred, E., S. Sathyendranath, and T. Platt. 2007. "Delineation of Ecological Provinces Using Ocean Colour Radiometry." *Marine Ecology Progress Series* 346: 1–13. doi:10.3354/meps07149.

EUM/MSG/ICD/105, 2013. MSG level 1.5 image data format description. Tech. rep., Darmstadt, Germany: EUMETSAT.

EUM/MTG/SPE/07/0036, 2010.MTG end-user requirements document [EURD]. Tech. rep., Darmstadt, Germany: EUMETSAT.

Gernez, P., D. Antoine, and Y. Huot. 2011. "Diel Cycles of the Particulate Beam Attenuation Coefficient under Varying Trophic Conditions in the Northwestern Mediterranean Sea: Observations and Modeling." *Limnology and Oceanography* 56: 17–36. doi:10.4319/lo.2011.56.1.0017.

Gibbons, D. E., and R. R. Richard. 1979. "Determination of Noise Equivalent Reflectance for A Multispectral Scanner: A Scanner Sensitivity Study." *NASA technical paper* 1575. Houston, Texas: Lyndon B. Johnson Space Center National Aeronautics and Space Administration.

Gordon, H. R., J. W. Brown, and R. H. Evans. 1988a. "Exact Rayleigh Scattering Calculations for Use with the Nimbus-7 Coastal Zone Color Scanner." *Applied Optics* 27: 862–871. doi:10.1364/AO.27.000862.

Gordon, H. R., O. B. Brown, R. H. Evans, J. W. Brown, R. C. Smith, K. S. Baker, and D. K. Clark. 1988b. "A Semi-Analytic Radiance Model of Ocean Color." *Journal of Geophysical Research: Atmospheres* 93: 10909–10924. doi:10.1029/JD093iD09p10909.

Gordon, H. R., and M. Wang. 1994. "Retrieval of Water-Leaving Radiance and Aerosol Optical Thickness over the Oceans with SeaWiFS: A Preliminary Algorithm." *Applied Optics* 33: 443–452. doi:10.1364/AO.33.000443.

Gregg, W. W., and N. W. Casey. 2004. "Global and Regional Evaluation of the SeaWiFS Chlorophyll Data Set." *Remote Sensing of Environment* 93: 463–479. doi:10.1016/j.rse.2003.12.012.

Hu, C., K. L. Carder, and F. E. Muller-Karger. 2001. "How Precise are SeaWiFS Ocean Color Estimates? Implications of Digitization-Noise Errors." *Remote Sensing of Environment* 76: 239–249. doi:10.1016/S0034-4257(00)00206-6.

Hu, C., L. Feng, and Z. Lee. 2013. "Uncertainties of SeaWiFS and MODIS Remote Sensing Reflectance: Implications from Clear Water Measurements." *Remote Sensing of Environment* 133: 168–182. doi:10.1016/j.rse.2013.02.012.

Hu, C., L. Feng, Z. Lee, C. O. Davis, A. Mannino, C. R. McClain, and B. A. Franz. 2012. "Dynamic Range and Sensitivity Requirements of Satellite Ocean Color Sensors: Learning from the Past." *Applied Optics* 51: 6045–6062. doi:10.1364/AO.51.006045.

IOCCG. 2008. "Why Ocean Colour? the Societal Benefits of Ocean-Colour Technology." In Eds. T. Platt, N. Hoepffner, V. Stuart, and C. Brown, IOCCG Report 7, pp. 141. Dartmouth, Canada.

IOCCG. 2012a. "Ocean-Colour Observations from a Geostationary Orbit." In Eds. D. Antoine, IOCCG Report 12, pp. 102. Dartmouth, Canada.

IOCCG. 2012b. "Mission Requirements for Future Ocean-Colour Sensors." In Eds. C. R. McClain and G. Meister, IOCCG Report 13, pp. 106. Dartmouth: Canada.

Jolivet, D., D. Ramon, P.-Y. Deschamps, F. Steinmetz, B. Fougnie, and P. Henry. 2007. "How the Ocean Color Product Quality Is Limited by Atmospheric Correction?" Proc. Envisat Symposium.

Lee, Z., and C. Hu. 2006. "Global Distribution of Case-1 Waters: An Analysis from SeaWiFS Measurements." *Remote Sensing of Environment* 101: 270–276. doi:10.1016/j.rse.2005.11.008.

Lee, Z., M. Jiang, C. Davis, N. Pahlevan, Y.-H. Ahn, and R. Ma. 2012. "Impact of Multiple Satellite Ocean Color Samplings in a Day on Assessing Phytoplankton Dynamics." *Ocean Science Journal* 47: 323–329. doi:10.1007/s12601-012-0031-5.

Loisel, H., V. Vantrepotte, K. Norkvist, X. Meriaux, M. Kheireddine, J. Ras, M. Pujo-Pay, et al. 2011. ""Characterization of the Bio-Optical Anomaly and Diurnal Variability of Particulate Matter, as Seen from Scattering and Backscattering Coefficients, in Ultra-Oligotrophic Eddies of the Mediterranean Sea."." *Biogeosciences* 8: 3295–3317. doi:10.5194/bg-8-3295-2011.

Mobley, C. D. 1994. *Light and Water: Radiative Transfer in Natural Waters*. London, UK: Academic press.

Morel, A., and S. Maritorena. 2001. "Bio-Optical Properties of Oceanic Waters: A Reappraisal." *Journal of Geophysical Research-Oceans* 106: 7163–7180. doi:10.1029/2000JC000319.

Morel, A., and L. Prieur. 1977. "Analysis of Variations in Ocean Color." *Limnology and Oceanography* 22: 709–722. doi:10.4319/lo.1977.22.4.0709.

Murakami, H. 2016. "Ocean Color Estimation by Himawari-8/AHI." In *SPIE Asia-Pacific Remote Sensing*, edited by Robert J. Frouin, Satheesh C. Shenoi, K. H. Rao, 987810–987810. doi:10.1117/12.2225422

Neukermans, G., K. Ruddick, E. Bernard, D. Ramon, B. Nechad, and P.-Y. Deschamps. 2009. "Mapping Total Suspended Matter from Geostationary Satellites: A Feasibility Study with SEVIRI in the Southern North Sea." *Optics Express* 17: 14029–14052. doi:10.1364/OE.17.014029.

Neukermans, G., K. Ruddick, and N. Greenwood. 2012. "Diurnal Variability of Turbidity and Light Attenuation in the Southern North Sea from the SEVIRI Geostationary Sensor." *Remote Sensing of Environment*: 564–580. 10.1016/j.rse.2012.06.003

O'Reilly, J. E., S. Maritorena, B. G. Mitchell, D. A. Siegel, K. L. Carder, S. A. Garver, M. Kahru, and C. McClain. 1998. "Ocean Color Chlorophyll Algorithms for SeaWiFS." *Journal of Geophysical Research: Oceans* 103: 24937–24953. doi:10.1029/98JC02160.

O'Reilly, J. E., S. Maritorena, D. A. Siegel, M. C. O'Brien, D. Toole, B. G. Mitchell, M. Kahru, et al. 2000. ""Ocean Color Chlorophyll a Algorithms for SeaWiFS, OC2, and OC4: Version 4." SeaWiFS Postlaunch Calibration and Validation Analyses." *Part, NASA Technical Memo* 3:9–23.

Pahlevan, N., Z. Lee, C. Hu, and J. R. Schott. 2013. "Analyzing Radiometric Requirements for Diurnal Observations of Coastal/Oceanic Waters from Geostationary Orbits." In *SPIE Defense, Security, and Sensing*, edited by Weilin W. Hou, Robert A. Arnone, 87240K–87240K. International Society for Optics and Photonics.

Peschoud, C., A. Minghelli, S. Mathieu, M. Lei, I. Pairaud, and C. Pinazo. 2016. "Fusion of Sun-Synchronous and Geostationary Images for Coastal and Ocean Color Survey Application to OLCI (Sentinel-3) and FCI (MTG)." *IEEE Journal of Selected Topics in Applied Earth Observations and Remote Sensing* 10 (1): 45–56.

Racault, M.-F., C. Le Quere, E. Buitenhuis, S. Sathyendranath, and T. Platt. 2012. "Phytoplankton Phenology in the Global Ocean." *Ecological Indicators* 14: 152–163. doi:10.1016/j.ecolind.2011.07.010.

Ruddick, K., G. Neukermans, Q. Vanhellemont, and D. Jolivet. 2014. "Challenges and Opportunities for Geostationary Ocean Colour Remote Sensing of Regional Seas: A Review of Recent Results." *Remote Sensing of Environment* 146: 63–76. doi:10.1016/j.rse.2013.07.039.

Ryu, J.-H., H.-J. Han, S. Cho, Y.-J. Park, and Y.-H. Ahn. 2012. "Overview of Geostationary Ocean Color Imager (GOCI) and GOCI Data Processing System (GDPS)." *Ocean Science Journal* 47: 223–233. doi:10.1007/s12601-012-0024-4.

Smayda, T. J. 1998. "Patterns of Variability Characterizing Marine Phytoplankton, with Examples from Narragansett Bay." *ICES Journal of Marine Science: Journal Du Conseil* 55: 562–573. doi:10.1006/jmsc.1998.0385.

Taylor, L., E. Boss, P. Brickley, D. Swift, R. Zaneveld, and P. Strutton. 2006. "Long Term Measurements of Physical and Optical Properties with Profiling Floats." In *Conference Poster inOcean Optics XVIII*, Montreal, Quebec.

Vanhellemont, Q., G. Neukermans, and K. Ruddick. 2014. "Synergy between Polar-Orbiting and Geostationary Sensors: Remote Sensing of the Ocean at High Spatial and High Temporal Resolution." *Remote Sensing of Environment* 146: 49–62. doi:10.1016/j.rse.2013.03.035.

Vanhellemont, Q., and K. Ruddick. 2015. "Advantages of High Quality SWIR Bands for Ocean Colour Processing: Examples from Landsat-8." *Remote Sensing of Environment* 161: 89–106. doi:10.1016/j.rse.2015.02.007.

Wang, M., W. Shi, and L. Jiang. 2012. "Atmospheric Correction Using Near-Infrared Bands for Satellite Ocean Color Data Processing in the Turbid Western Pacific Region." *Optics Express* 20: 741–753. doi:10.1364/OE.20.000741.

Werdell, P. J., and S. W. Bailey:. 2005. "An Improved In-Situ Bio-Optical Data Set for Ocean Color Algorithm Development and Satellite Data Product Validation." *Remote Sensing of Environment* 98: 122–140. doi:10.1016/j.rse.2005.07.001.

Wilson, R. T. 2012. "Py6s: A Python Interface to the 6s Radiative Transfer Model." *Computers and Geosciences* 51: 166–171. doi:10.1016/j.cageo.2012.08.002.